

# Coronal mass ejections and the associated activities on the solar disk observed on October 26, 2003

X. Bao<sup>1</sup>, H. Zhang<sup>1</sup>, J. Lin<sup>2,3</sup>, and G. A. Stenborg<sup>4</sup>

<sup>1</sup> National Astronomical Observatories of China, Chinese Academy of Sciences, Beijing 100012, PR China  
e-mail: [xbao@bao.ac.cn](mailto:xbao@bao.ac.cn)

<sup>2</sup> Yunnan Astronomical Observatory, National Astronomical Observatories of China, Chinese Academy of Sciences, Kunming, Yunnan 650011, PR China

<sup>3</sup> Harvard-Smithsonian Center for Astrophysics, 60 Garden Street, Cambridge, MA 02138, USA

<sup>4</sup> Department of Physics, Catholic University of America, 620 Michigan Avenue, Washington, DC 20064, USA

Received 21 April 2006 / Accepted 6 September 2006

## ABSTRACT

**Aims.** Coronal mass ejections (CMEs) are usually considered fast (slow) if their velocities are greater (less) than  $500 \text{ km s}^{-1}$ . It is generally believed that fast CMEs are well associated with activity manifested on the solar disk, such as solar flares, and that slow CMEs are often associated with filament eruptions out of active regions and can hardly leave any signature on the solar disk. However, this may not be totally true for the cases we are studying in the present work, where we have explored more explicitly than in previous studies the relationship between different types of CMEs and the associated on-disk activities.

**Methods.** We analyzed four CMEs that happen to take off near the west limb of the Sun on October 26, 2003. Their maximum speeds varied from  $300$  to  $1800 \text{ km s}^{-1}$ , with average accelerations from about  $6 \text{ m s}^{-2}$  up to  $330 \text{ m s}^{-2}$ . They span over almost the full range of speeds of typical CMEs, from slow to fast. The evolution and kinematical properties of each CME at their early stages as well as the corresponding processes on the solar disk are examined.

**Results.** Three out of the four events analyzed, including slow and fast ones, exhibited apparent acceleration during their early development and a likely association with solar disk activity as manifested by ribbon flares and post-event loops. The fourth event (the CME that did not show any clear association with solar disk activity) was not the slowest one: it had a median speed ( $\leq 400 \text{ km s}^{-1}$ ). This suggests that some existing conclusions about the CME-flare correlation need to be re-investigated. In addition, the correlation of the coronal mass ejection angular widths to their speeds is also discussed.

**Key words.** Sun: coronal mass ejections – Sun: filaments – Sun: flares – Sun: activity

## 1. Introduction

Coronal mass ejections (CMEs) are transient phenomena in the solar corona that expel a large amount of plasma and magnetic flux into interplanetary space. Since the first observations made by the space-borne coronagraph on board the Orbit Solar Observatory-7 (Tousey 1973) and Skylab (Gosling 1974) in the early 1970s, CMEs have become one of the most extensively studied topics in solar physics. This is partly because they have opened a new window to understanding traditional solar phenomena such as solar flares and eruptive prominences, but also because they are often the cause of significant impacts on the Earth geomagnetic environment, our technology, and eventually humans in space. This topic has become so important that a specific name was assigned to describe it, namely Space Weather (Klimchuk 2001).

Both observations and theories suggest that i) CMEs are involved in the reorganization of large scale magnetic fields in the corona; ii) CMEs are closely related to eruptive activities on the solar disk (e.g., solar flares and eruptive prominences, see Forbes 2000; Priest & Forbes 2002; Lin et al. 2003); and iii) CMEs are often correlated to disruptions of helmet streamers above the solar limb (e.g., see Raymond et al. 2003, and references therein). It has been established for more than two decades that the association between flares and CMEs exists (Munro et al. 1979). However, the careful analysis of CME/flare events show

that their spatial and temporal relationships are much more complicated than expected. In particular, the characteristic angular size of CMEs is about several times larger than the associated  $H\alpha$  flares and the relevant active regions (Hundhausen 1988; Harrison 1991). Lin (2004) and Lin et al. (2004) pointed out that such a difference in size between flares and the associated CMEs results from the difference in the plasma environments where they develop. As for the time correlation between CMEs and solar flares, Harrison (1995) found that the onset of CMEs usually preceded the onset of the associated flares by tens of minutes. More recently, Zhang et al. (2001) concluded that the initial stage of CMEs is prior to the flare onset. Moreover, Zhang et al. (2002) showed that the faster the CME, the earlier the associated flare reaches its peak intensity, and that the association of fast CMEs with flares is better and more apparent than that of slow CMEs.

CMEs are also related to eruptive prominences. Gilbert et al. (1999) found that about 94% of the eruptive prominences are associated with CMEs. Early CME studies indicate that the filament-associated CMEs are often slow and the flare-associated CMEs are usually fast (Gosling et al. 1976). MacQueen & Fisher's (1983) showed that the flare-associated CMEs exhibit little acceleration with height, while the eruptive prominence-associated events exhibit large acceleration. They suggested that two different physical processes were present.

Andrews & Howard (2001) points out that there are two types of CMEs: i) one characterized by a constant acceleration; and ii) another one characterized by constant speed. By means of a statistical study Moon et al. (2002) showed that fast CMEs tend to decelerate while slow ones tend to accelerate. However, recent case studies on CMEs are not consistent with that result (Dere et al. 1999; Zhang et al. 2004). Vršnak et al. (2005) presented a statistical investigation of LASCO CMEs and found that the flare-associated and non-flare-associated CMEs show quite similar characteristics, in contradiction with the concept of two distinct types of CMEs. We point out that the statistical studies mentioned above used data from both LASCO C2 and C3 coronagraphs. Their FOV start at  $2 R_{\odot}$ , where many, if not most, CMEs have likely finished their main acceleration phase (St. Cyr et al. 1997). Therefore, whether there are two distinct classes of CMEs is still an open question.

CMEs are also often observed to take off from regions above helmet streamers (Sheeley et al. 1982). These CMEs usually develop after a pre-existing streamer starts swelling and eventually disappears. Sheeley et al. (1982) first named such eruptive processes as “streamer blowouts”. Howard et al. (1985) found that such CMEs were typically slower than other CMEs. Hundhausen (1993) concluded that these kind of CMEs were often associated with disruptions of streamer structures that manifest the large-scale closed magnetic structure. The general picture of the pre-event coronal structure as a helmet streamer with lower-density cavity containing a flux rope and dense prominence seems to fit at least some CME observations (Plunkett et al. 2002; Gopalswamy et al. 2004). However, Subramanian et al. (1999) studied the relationship between CMEs and helmet streamers, and found that 73% of the investigated CMEs had no effect on the helmet streamer, only 16% caused the helmet streamer to disrupt. Obviously, their result is different from the general scenario displayed earlier.

Six events that occurred on October 26, 2003 provided us with a set of nice samples to investigate the various CME types discussed above. Briefly, on that day the following events were registered by instruments on board the Solar and Heliospheric Observatory (SOHO): i) two CMEs starting with corresponding eruptive prominences in a spotless region near the west limb; ii) a CME from active region (AR) 10486; iii) a CME from the east limb; iv) a CME developing from above a helmet streamer on NW; and v) a wide CME event on W from AR 10484. Among the six CME events, the CME from AR 10486 is similar to the CME from AR 10484 both in its kinematical properties as well as on its associated solar disk activity. The CME from the east limb is associated with activity on the backside of the Sun. Hence, in this study we examine the remaining four CME events from the west limb. These four events were selected not only because they occurred successively within a single day, but also because they represent three types of CMEs with different origin (namely eruptive prominence, flare, and streamer blowout), initiation, propagation, and also probably different physical processes involved. We outline our observational data in general in the next section, give the results obtained from these data in Sect. 3, and discuss our results in Sect. 4.

## 2. The Observations

To explore the evolution of the four events mentioned above, we employ observations of the solar disk in  $H\alpha$  and EUV, and coronagraph observations in white-light. The former gives us a view of the activity on the solar disk, such as flares and eruptive prominences by the time prior to and during the development of

the CME event, while the latter are used to track the events further out. The  $H\alpha$  images were obtained from the Huairou Solar Observing Station (HSOS) with a cadence of 5 min.

The EUV images used were from the EIT instrument on board *SOHO*. The full disk EIT images in 195 Å with spatial resolution of  $2''/\text{pixel}$  provide us a view of the evolution of CMEs in the lower corona. We applied the wavelet-based intensity contrast-enhancement (WICE) technique (Stenborg & Cobelli 2003, and references therein) to those images so that the fine detail structure of the filaments involved (such as their helical structure) can be better seen. In addition, faint ribbon flares can be easily distinguished as well.

The WICE technique was developed by Stenborg & Cobelli (2003) for multiresolution image processing, and is applicable to any 2D data set to enhance both boundaries and internal details of originally faint and diffuse structures. The method implemented employs a multi-level decomposition scheme (splitting algorithm of a wavelet packet on non-orthogonal wavelets) via the à trous wavelet transform, local noise reduction and interactive weighted recomposition. This approach represents a major advance towards unambiguous image interpretation and provides a means for the quantification of stationary and dynamic coronal structures required for conducting morphological studies. The detailed descriptions and discussions about this technique can be found in the works by Starck et al. (1997) and by Stenborg & Cobelli (2003).

In order to follow the evolution of the CME events at coronal heights, coronagraph data were used. In particular, the low white light K-corona ( $1.08$  to  $2.85 R_{\odot}$ ) is covered with images of the MK4 coronagraph with a 3 min cadence (where the leading edge of the CME usually starts to form, see also Bao et al. 2006). The white light images from LASCO C2 (with a cadence of 12 min)<sup>1</sup> and C3 (with cadence of about 30 min), cover the distance from 2 to  $30 R_{\odot}$ , and provide an extensive view of CME evolution from the middle to the outer corona. They enable us to obtain the height-time profiles of the CME events extending up to 30 solar radii. The height of the CMEs at any given instant was calculated from the outermost point of the leading edge to the heliospheric center in the snapshots of CMEs images. Because the four CMEs occurred near the west limb, projection effects are not very severe. The velocity of CMEs after projection correction could be obtained by  $v = v_p / \cos \theta$ , where  $v_p$  is the velocity projected on the plane of the sky and  $\theta$  is the angle between the radial direction of their source regions and the plane of the sky. In addition, the magnetograms taken by the Michelson Doppler Imager (MDI) on board *SOHO* are also used to help analyze the corresponding  $H\alpha$  and EUV images of the same objects.

## 3. The events

Four events on October 26, 2003 are the subject of this section. Namely, i) the eruption of a long filament at about 00:36 UT originally located near the SW limb with its centroid at around S17W55 (hereafter Event 1); ii) the eruption of a short filament starting at about 01:13 UT originally located near the W limb with its centroid at around S01W63 (hereafter Event 2); iii) a slow CME ( $<400 \text{ km s}^{-1}$ ) with no discernible on-disk signatures that sprouted from a pre-existing helmet streamer located over the NW limb that was observed to take off at 08:00 UT (hereafter Event 3); and iv) an X1.2 X-ray flare

<sup>1</sup> Interested readers may find the wavelet-enhanced C2 movies at: <http://lasco-www.nrl.navy.mil/wavelet> for comparison.

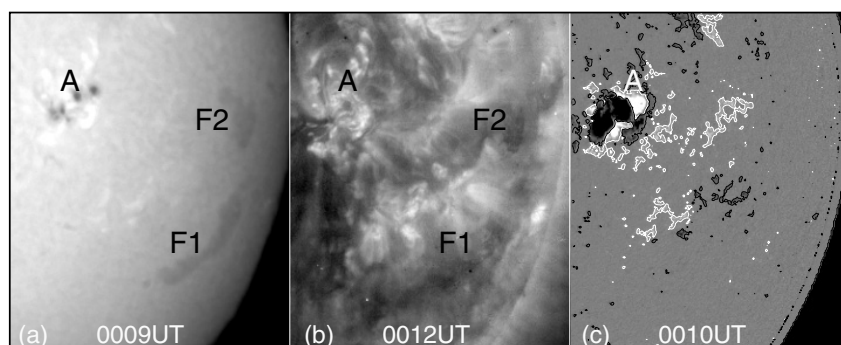


**Fig. 1.** Various features observed on the solar disk near the west limb by different instruments early on October 26, 2003: **a)**  $H\alpha$  image at 00:09 UT, **b)** EIT 195 Å image at 00:12 UT, **c)** MDI longitudinal magnetogram at 00:10 UT – the white (black) patches represent positive (negative) polarities, contour levels at  $\pm 60$  Gauss. The active region AR 10484 with  $\beta - \gamma - \delta$  magnetic configuration is indicated by A, and the two filaments by F1 and F2, respectively.

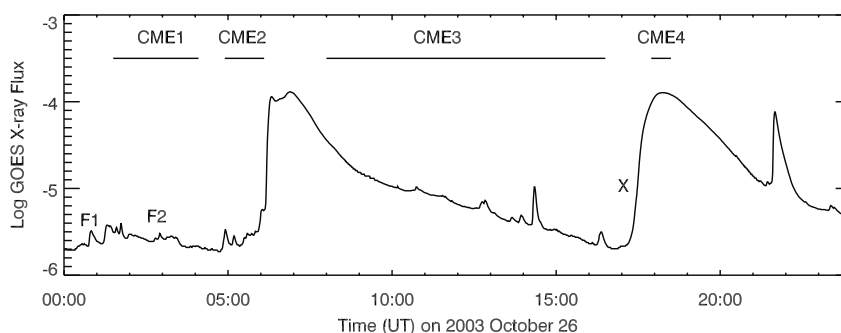


**Fig. 2.** Plot of the GOES X-ray flux in the lower energy channel (1–8 Å) versus time on October 26, 2003. The horizontal solid lines mark the time interval when the CMEs are visible in the field of view of LASCO C2. The onset time of the eruption of filaments F1 and F2, as well as that of the X1.2 X-ray flare are indicated by F1, F2, and X respectively. No on-disk activity associated with CME3 was detected.

on NOAA AR 10484 (N05W29) that started at 17:24 UT with a fast CME associated ( $>1800 \text{ km s}^{-1}$ ) (hereafter Event 4).

Figure 1 shows a region of the solar disk near the W limb as seen by three different instruments early on October 26, 2003: i) an  $H\alpha$  image recorded by HSOS at 00:09 UT (Fig. 1a); ii) an EIT 195 Å subframe taken at 00:12 UT (Fig. 1b); and iii) the corresponding MDI magnetogram obtained at 00:10 UT (Fig. 1c). A long and a short filament (denoted as F1 and F2, respectively, and hereafter) can be seen in the figure. They are the solar counterparts of Events 1 and 2, respectively. The active region AR10484 (on-disk counterpart of Event 4) with a complex  $\beta - \gamma - \delta$  magnetic configuration appears denoted as A in Fig. 1).

The GOES X-ray flux over the range from 1 to 8 Å on October 26, 2003 is shown in Fig. 2. The period when each of the four CMEs showed up in the C2 FOV is marked by a horizontal solid line. The onset times of F1 and F2 eruptions, and the X1.2 flare are indicated by F1, F2 and X, respectively. We display in the following subsections the detailed results of the analysis of the above four events. The focus is on the surface activity, CME propagation, and evolution of the morphological features of each eruption.

### 3.1. Event 1: CME associated with the eruption of the long filament

The first event near the west limb on October 26, 2003 began with the eruption of a long filament (F1). Figure 3 displays a time sequence of the event as recorded by the EIT and LASCO instruments. The EIT 195 Å frames were post-processed with the WICE technique in order to make more visible the details

of the fine structure of the filament, ribbon flare, and post-event loops<sup>2</sup>.

The central part of the filament F1 is seen to lift slowly during the first half hour (00:00–00:36 UT). From 00:36 UT on, the rising of the filament speeds up significantly. The upward motion of the central part of F1 is much faster than the other parts, so the filament develops an arch shape. The southern leg of F1 remains visible, and the shape of F1 became round forming an  $\Omega$  shape by 01:13 UT (arrow F1 in Fig. 3c). With the filament erupting, two bright ribbon flares (indicated by arrow R1 in Fig. 3c) start to be discernible (01:13 UT) at both sides of the location where F1 was initially located. As time passes by, they become brighter. They separate from each other after 02:00 UT (arrow R1 in Fig. 3e). A group of post-event loops joining the two bright ribbons (arrow L1 in Fig. 3f) are seen to grow starting at 02:24 UT, just before the brightness of the two ribbons reaches maximum intensity at 03:12 UT (arrow R1 in Fig. 3g).

The leading edge of the CME (hereafter CME1) associated with the eruption of F1 first appears in the LASCO C2 FOV above the W limb at 01:31 UT (indicated by arrow E in Fig. 3k). Its propagation is slow (arrow E in Fig. 3l). A bright core (indicated by arrow C in Fig. 3l) appears in C2 at 02:30 UT, following the leading edge of CME1. The core structure looks like a loop by 04:06 UT (arrow C in Fig. 3m), resembling the appearance of the filament F1 shown in Fig. 3c. For completeness, Figs. 3p through 3t show the development of CME1 in the FOV of LASCO C3. Note that the event is surpassed in the C3 FOV by Event 2 (see next subsection).

<sup>2</sup> The corresponding gif movie is available at <http://sun10.bao.ac.cn/staff/baoxm/031026.gif>

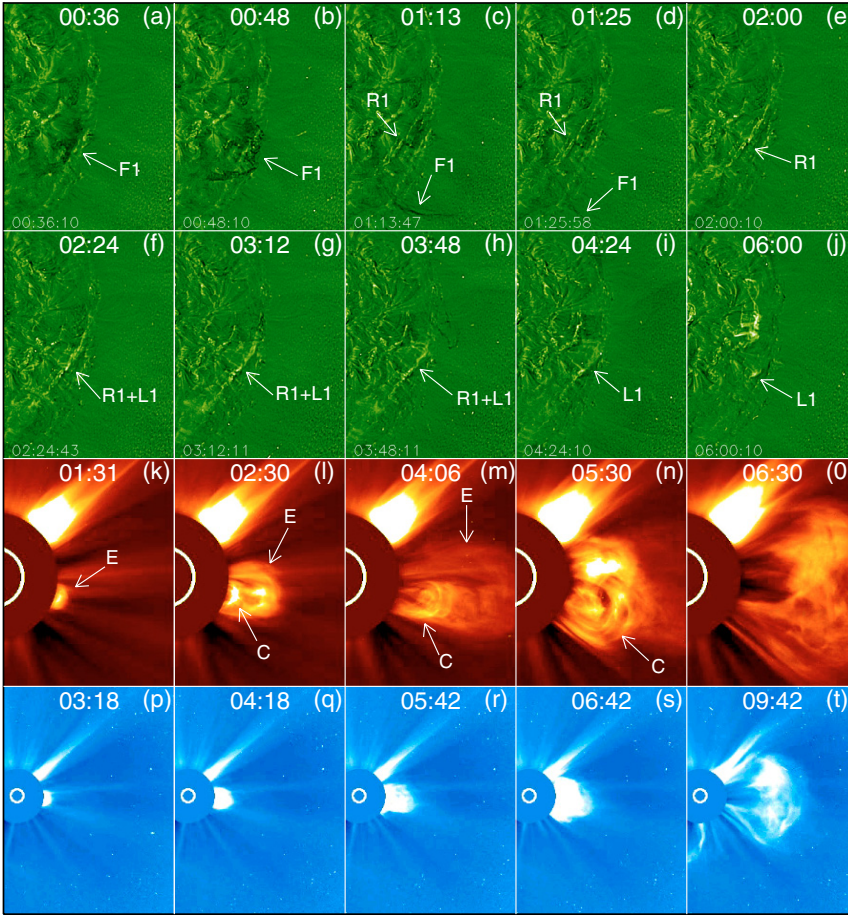


**Fig. 3.** EIT and LASCO C2/C3 time sequence of Event 1. The EIT 195 Å images (*upper two rows*) show the eruptive process of filament F1 (indicated by arrow F1) in the lower corona. The WICE technique was used to enhance fine structures of filaments and flare ribbons. When the filament F1 reached certain height, flare-ribbons appeared at the two sides of the place where F1 used to sit (indicated by the arrow R1). They later connected themselves by loops (indicated by the arrow L1). The LASCO C2 and C3 white light images (*lower two rows*) show the development of CME1 between 2 and 30  $R_{\odot}$ . The leading edge of CME1 is pointed out with the arrow E, while the core is indicated by the arrow C.

Due to the non-radial motion of CME1, we use the time profile of the distance between the farthest point at its leading edge and the line connecting the north pole to the south pole to depict its motion. However, the height of F1 is still measured as the distance from the initial location of its center M at 00:00 UT (i.e., before the eruption) to the instantaneous farthest point N. Figure 4a shows the height-time profile as projected on the plane of sky of both F1, and leading edge and core of the associated CME in the C2 FOV. The corresponding velocity and acceleration profiles are shown in Figs. 4b and 4c, respectively.

The solid lines in Fig. 4 plot the results of fitting the data to the model given by

$$h(t) = a_0 + a_1 t + a_2 t^2 e^{-a_3 t}, \quad (1)$$

where  $h$  is the height of the CME core (or F1) in units of solar radius,  $t$  is the time in hours with  $t = 0$  corresponding to 00:00 UT, and  $a_i$  are the coefficients determined by least squares that best fit the model to the data. Their value is given in Cols. 2–5 of Table 1.

We observe in Fig. 4a that the projected height of the CME core at different times follows that of the F1 filament. This fact strongly suggests that the CME core can be identified with the associated erupting filament.

The velocity of the different parts of CME1 (leading edge, core) is obtained by taking the derivative of  $h(t)$  in Eq. (1) with respect to  $t$ . By taking the derivative twice, the acceleration profile is obtained. The corresponding curves are plotted in Figs. 4b and 4c, respectively. We notice that the maximum speed of F1 was about  $200 \text{ km s}^{-1}$ , and the acceleration decreases from around  $50 \text{ m s}^{-2}$  to around  $-15.6 \text{ m s}^{-2}$ . The maximum acceleration is given in Col. 6 of Table 1.

In addition, Fig. 4a also plots the heights of the CME1 leading edge (marked as diamonds) versus time for comparison. These data are fitted by a quadratic function (1) with  $a_3 = 0$ . The dashed lines in Fig. 4 plot the fitting results of CME1 height-time data according to the quadratic function, which indicates that the leading edge of CME1 expanded at a constant acceleration of  $15.9 \text{ m s}^{-2}$ . Its average speed in the plane of the sky was about  $315 \text{ km s}^{-1}$ , which reached up to  $390 \text{ km s}^{-1}$  after the projection correction has been made.

### 3.2. Event 2: CME associated with the eruption of the short filament

The second event begins with the eruption of the short filament (F2). A time sequence of the event as observed in EIT 195 Å and LASCO C2 and C3 images is shown in Fig. 5. The arrow F2 in the upper row of the figure points out the filament. The filament F2 starts to lift at around 01:13 UT (arrow F2 in Fig. 5c), just after the eruption of F1 began. It rises slowly until around 03:24 UT, when it adopts the form of a small arch (arrow F2 in Fig. 5d). By that time, it starts to move faster, and by 03:48 UT appears as a relaxed rope above the solar limb (arrow F2 in the Fig. 5e).

The flare ribbons (arrow R2 in Fig. 5e) appear when F2 reaches a height of 290 Mm (03:48 UT), about two and a half hours after the onset of F2 take-off. The post-event loops anchored at the flare ribbons become visible by 05:48 UT (arrow L2 in Fig. 5h), after the brightness of the flare ribbons reach maximum intensity at 05:12 UT (arrow R2 in Fig. 5g).

**Table 1.** Coefficients  $a_i$  for the four CMEs.

Object	$a_0$	$a_1$	$a_2$	$a_3$	Acceleration ( $\text{m s}^{-2}$ )	Time in UT at $t = 0$
CME1/core	1.063	-0.412	0.806	-0.260	52.3	00:00
CME1/LD	1.061	0.785	0.147	0	15.9	00:00
CME2/core	1.191	-0.465	0.326	0	35.2	00:12
CME2/LD	1.043	1.077	0.147	0	15.4	00:12
CME3	3.839	0.529	0.051	0	5.6	07:31
CME4	1.43	3.530	3.133	0.350	330	17:28

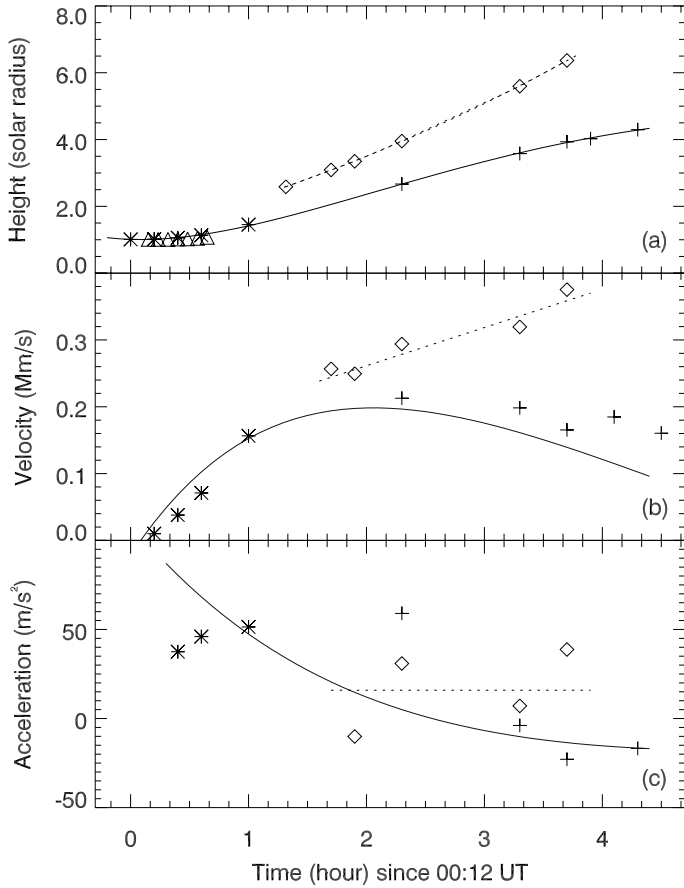


**Fig. 4.** **a)** Height-time, **b)** velocity-time, and **c)** acceleration-time profiles of CME1 leading edge ( $\diamond$ ) in the C2 FOV, and filament F1 in the FOV of i) EIT 195 Å ( $*$ ); ii) H $\alpha$  ( $\Delta$ ); and iii) LASCO C2 (core of CME1,  $+$ ) images. The solid line indicates the fitting result to the F1 height-time data according to Eq. (1), the dashed line indicates the quadratic fitting based on Eq. (1) to the CME1 height-time data for  $a_3 = 0$ . The time of  $t = 0$  for fittings is 00:00 UT.

The leading edge of the CME (hereafter CME2) associated with the F2 eruption starts to be seen in the FOV of C2 at 05:30 UT, above the W limb (arrow CME2 in Fig. 5n). It quickly catches up with the trailing part of CME1, so it becomes then difficult to disentangle both events. The leading edge of CME2 quickly reaches the outer edge of the C2 FOV (05:54 UT), and by 06:30 UT is already well past its outer edge (Fig. 5o). By that time, CME2 has an angular span of about  $73^\circ$ , almost as twice as that of CME1 (just  $37^\circ$ ). The leading edge of CME2 (arrow CME2 in Fig. 5q) is first seen in C3 at 05:42 UT, following the leading edge of CME1 (arrow CME1 in Fig. 5q). The leading edge of CME2 catches up with that of CME1 some time between 06:42 UT (Fig. 5r) and 07:42 UT (Fig. 5s). The

two CMEs continue to propagate westward as a single CME after 09:42 UT (Fig. 5t).

Figure 6a plots the height-time profile of F2. Figure 6b shows that CME2 propagated nearly at a constant speed,  $\sim 627 \text{ km s}^{-1}$ , which was almost twice of that of CME1. Actually the average speed of CME2 is about  $724 \text{ km s}^{-1}$  after projection correction has been made. In Fig. 6c, CME2 showed the small acceleration ( $\sim 15.4 \text{ m s}^{-2}$ ) after it appeared in FOV of C2 ( $>4 R_\odot$ ), while F2 underwent the apparent acceleration ( $\sim 35.2 \text{ m s}^{-2}$ ) in the early stage ( $1-5 R_\odot$ ).

### 3.3. Event 3: disruption of a helmet streamer resulting in a slow CME

The third event develops as a slow CME (hereafter CME3) with the disruption of a helmet streamer. The upper and middle row of Fig. 7 show a C2 time sequence of the event, while the last row of the figure shows the event as seen by C3. CME3 takes about 8 h to sweep the FOV of C2 and another 12 h to sweep the FOV of C3. There was no significant changes in the X-ray flux prior to and during the development of this event. Likewise, H $\alpha$  and EIT 195 Å images did not registered any significant activity that could be associated to the event.

The helmet streamer on NW starts to sway after being slightly deflected by CME2 at around 05:00 UT (see Figs. 5k through 5t). Then by 08:06 UT, it is seen to swell (Fig. 7a), and finally, apparently by 11:06 UT, starts to expand (Fig. 7b). Compared with the helmet streamer, the other leg of this arcade was too faint to be seen prior to the eruption, and it became visible somehow during the eruption.

The morphological features of the helmet streamer shown in the FOV of C3 start to change by 11:18 UT (Fig. 7i). However, the above large arcade could not be seen as a whole structure in the C3 FOV until 15:18 UT (Fig. 7j). By this time, the angular span slowly increases to about  $80^\circ$  (Fig. 7k). After 18:18 UT, CME3 continues to bulge while the angular span increases to more than  $90^\circ$ . The northern leg of CME3 is seen to become fainter faster than the southern leg. After 22:18 UT, the northern leg almost totally disappears in the C3 FOV while the southern leg resembles a trumpet-like structure (Fig. 7l).

Figure 8a plots the variations of CME3 heights versus time, and Figs. 8b and 8c plot the corresponding velocities and accelerations. It shows that CME3 expanded very slowly as it was in the altitude range covered by FOV of C2. The average velocity at this stage was less than  $40 \text{ km s}^{-1}$ . But its motion became apparently faster after entering FOV of C3 with an average velocity of about  $300 \text{ km s}^{-1}$ . The fitting acceleration is about  $5.6 \text{ m s}^{-2}$  deduced from the fitting results.

### 3.4. Event 4: CME associated with an X1.2 X-ray flare

The fourth event developed as a fast CME associated with an X1.2 X-ray flare on AR 10484, which was a  $\beta - \gamma - \delta$

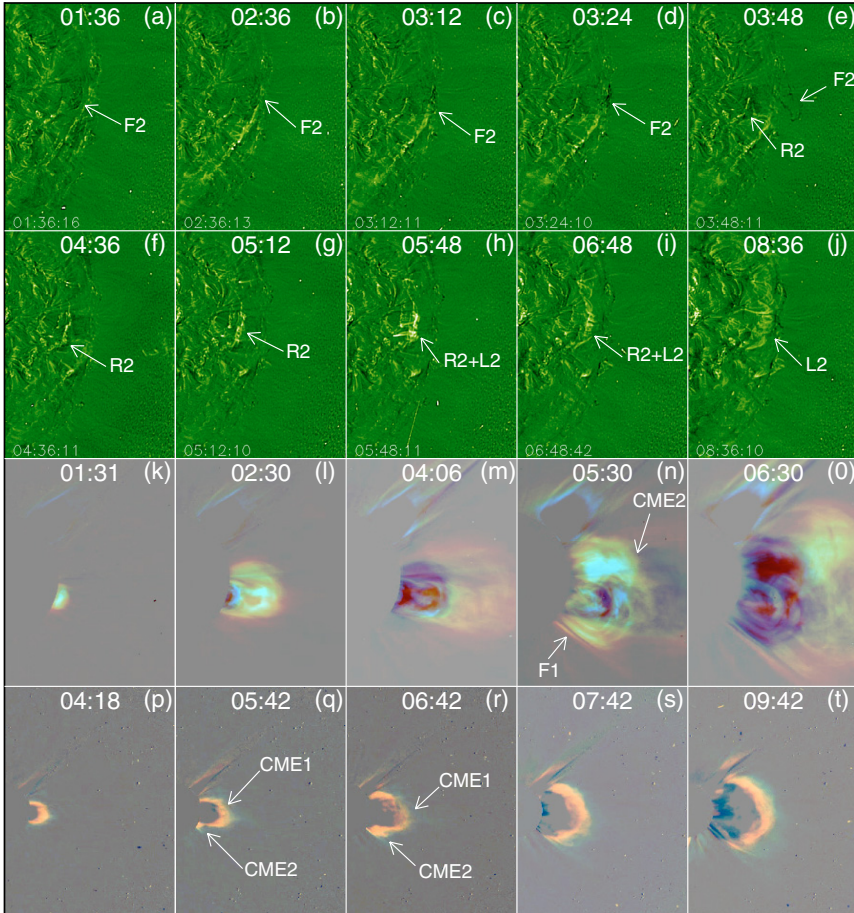


**Fig. 5.** EIT and LASCO C2/C3 time sequence of Event 2. The EIT 195 Å images (*two upper rows*) show the eruption of filament F2 (indicated by the arrow F2) in the lower corona. Two flare ribbons (indicated by the arrow R2) and a group of post-flare loops (indicated by the arrow L2) appeared near the location where the F2 sat. The LASCO C2 and C3 running difference images (*two lower rows*) show how CME2 (arrow marked CME2) expanded and interacted with the core of CME1 (arrow marked F1) and the leading edge of CME1 (arrow marked CME1).

region located around N05W29. The X-ray flare occurred between 17:21–19:21 UT with peak emission at 18:19 UT. Before the major eruption took off, small scale activity (translated into minor eruptions) in and around AR 10484 never ceased, as observed in EIT 195 Å images in the time period that starts on previous day through the onset of the major eruption (see Fig. 9). The small scale activity includes brightenings of the local magnetic structure in AR 10484, bright and dark material jets guided by the local magnetic fields, a larger jet (compare e.g. Figs. 9c and 9d) as well as several changes in the local magnetic fields (compare e.g. Figs. 9e and 9f).

The most significant increase in brightness in EIT 195 Å starts at 17:24 UT in the region between the markers R1 and R2 shown in Fig. 9h. It expands outward by 17:48 UT, reaching maximum intensity at around 18:48 UT. Frames h through l in Fig. 9 show the brightening taking place at the footpoint and the top of flare loops. Afterward, a group of bright loops begin to be seen.

The early stage of the CME associated to the X-ray flare event (hereafter CME4) was recorded by the MK4 coronagraph. The corresponding time sequence of its early development in the lower corona is shown in Fig. 10. A slight variation in brightness can be discerned above the W limb in the MK4 images by 17:25 UT, just after the start of the ascending phase of the flare (17:24 UT). A faint leading edge can be identified at about  $0.3 R_{\odot}$  above the west limb at 17:28 UT (indicated by an arrow in Fig. 10a). The fan-like leading edge of CME4 (also indicated by an arrow in Fig. 10b) becomes clearly visible at 17:31 UT (at  $0.46 R_{\odot}$ ) with an angular span of about  $53^{\circ}$ . The leading edge of the event adopts then a clear

semi-circular shape, its angular width increasing up to  $107^{\circ}$  just 6 min later, i.e., by 17:31 UT (pointed out with an arrow in Fig. 10c). Afterward, the event continues expanding slowly, reaching an angular span  $117^{\circ}$  by 17:43 UT (Fig. 10d). LASCO C2 and C3 images of the event (not shown here) indicate that CME4 spanned more than  $130^{\circ}$  after 18:54 UT. CME4 was cataloged as a partial halo event in the CDAW LASCO CME catalog<sup>3</sup>.

We measured the projected height of CME4 from the heliospheric center to the farthest point of the expanding arcade. Figure 11 plots the heights (a); velocity (b); and acceleration (c) of the leading edge as projected onto the plane of the sky. Figure 11b suggests that the leading edge of CME4 propagated with an initial speed of about  $\sim 500 \text{ km s}^{-1}$ , reaching a speed of about  $1100 \text{ km s}^{-1}$  within a half hour – an initial acceleration of  $330 \text{ m s}^{-2}$ . Figure 11c shows that the acceleration stage of CME4 lasted about one hour. After the CME reached a height of  $5 R_{\odot}$ , all points were located (within the error) on a single straight line. This fact clearly suggests that CME4 propagated nearly at a constant velocity (at least during its development in the C3 FOV). The slope of this straight line brings the speed of CME4 to  $1466 \text{ km s}^{-1}$ , and the correction to the projection effect leads to  $1827 \text{ km s}^{-1}$ .

#### 4. Discussions and conclusions

We have studied four events that occurred successively on the west limb of the solar disk within one day. Each event was seen

<sup>3</sup> See [http://cdaw.gsfc.nasa.gov/CME\\_list/](http://cdaw.gsfc.nasa.gov/CME_list/)

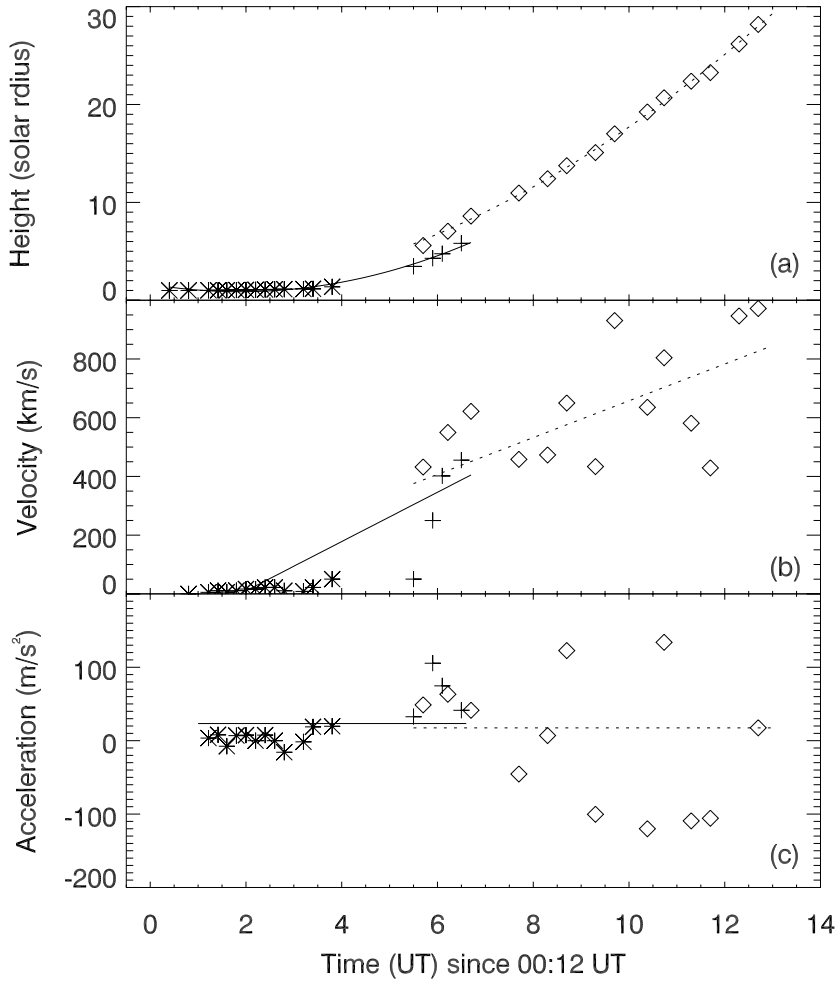


**Fig. 6.** **a)** Height-time, **b)** velocity-time, and **c)** acceleration-time profiles of 1) F2 in the FOV of i) EIT 195 Å (\*); and ii) C2 (core of CME2, +); and 2) the leading edge of CME2 in the FOV of C2 and C3 images ( $\diamond$ ). The solid (dashed) lines specify the quadratic fitting to the F2 (the leading edge of CME2) height-time data. The time  $t = 0$  corresponds to 00:12 UT.

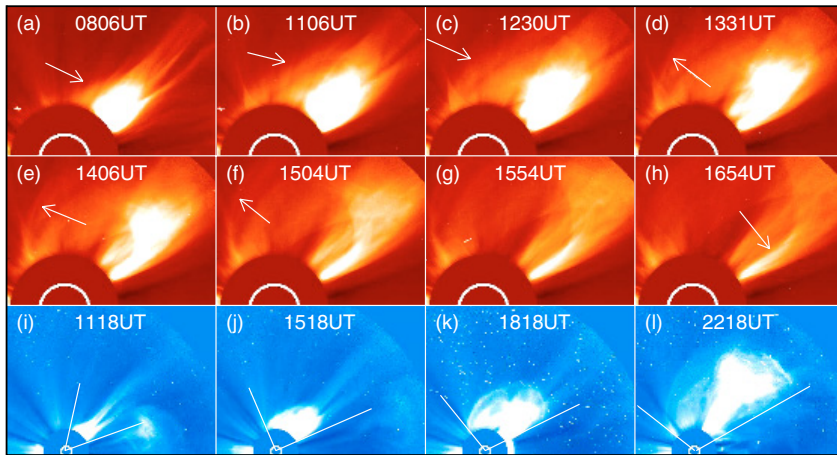


**Fig. 7.** LASCO C2 (upper two rows) and C3 (bottom row) time sequence of the disruption of a helmet streamer on October 26, 2003. The white arrows in **a)–f)** indicate the expanding part (leg) of the streamer, while the shape and profile of the other leg remained almost unchanged (white arrow in **h)**). The angular span of the CME-associated magnetic arcade is marked by two straight lines in the C3 frames.

in the LASCO coronagraphs as a discrete coronal mass ejection (CME). They all exhibited distinct morphological features (size, width, shape), kinematical properties (speed, acceleration), and origin (spotless regions, active regions). In particular, both CME1 and CME2 were associated with eruptive prominences, two-ribbon flares in EIT 195 Å and very weak X-ray flares (classes C3.8 and C2.2, respectively), but were not associated with any  $H\alpha$  flare. CME3 sprouted from a helmet streamer that had existed since long before the event took place. Careful analysis of its development indicated that a large scale magnetic arcade was involved, the helmet streamer being associated with one of the legs of this arcade. No on-disk activity was observed

prior to or during the development of this event. The fourth event happened to be the most energetic one, involving an X1.2 X-ray flare and a fast and very wide CME (CME4). The main characteristics of the four events are summarized in Table 2. It is worth noting that although the height range of CME3 acceleration was up to  $30 R_{\odot}$ , the average acceleration of CME3 was only  $5.6 \text{ m s}^{-2}$ .

St. Cyr et al. (1991) have speculated that slow CMEs are poorly associated with other solar activities simply because any  $H\alpha$ , X-ray and/or radio signatures are too weak and lie below the sensitivity threshold of actual instruments. On the other hand, the EIT 195 Å images can provide a more sensitive view of the

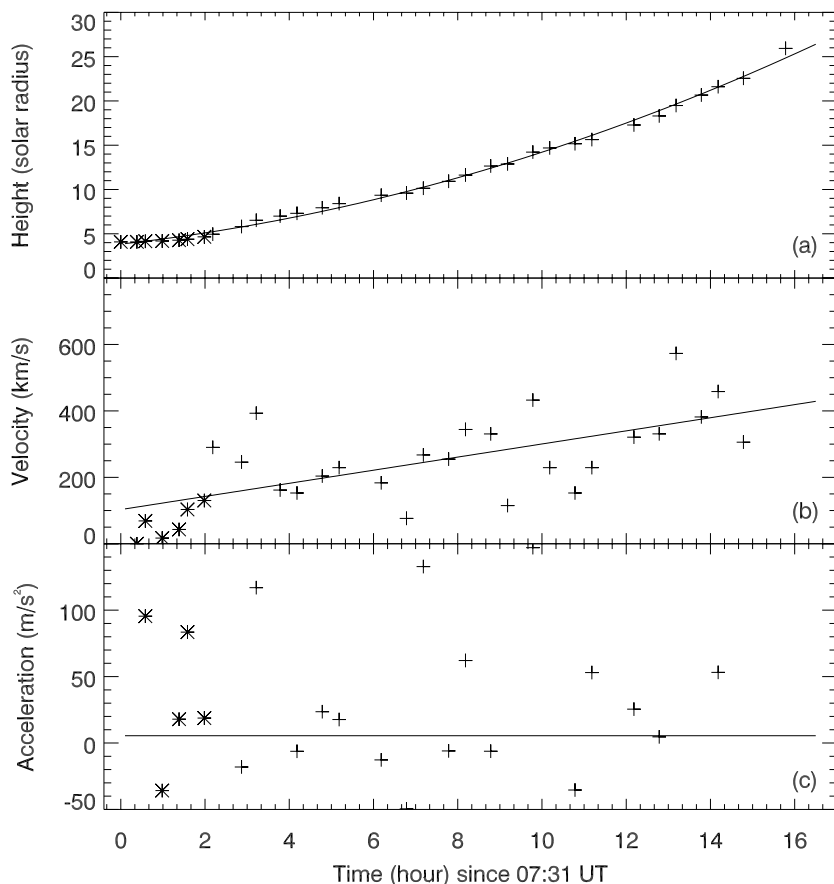


**Fig. 8.** a) Height-time, b) velocity-time, and c) acceleration-time profile of CME3 appearing in FOV of C2 (\*) and C3 (+), respectively. The solid line in indicates the quadratic fitting result on the basis of Eq. (1) for  $a_3 = 0$  with  $t = 0$  corresponding to 07:31 UT.

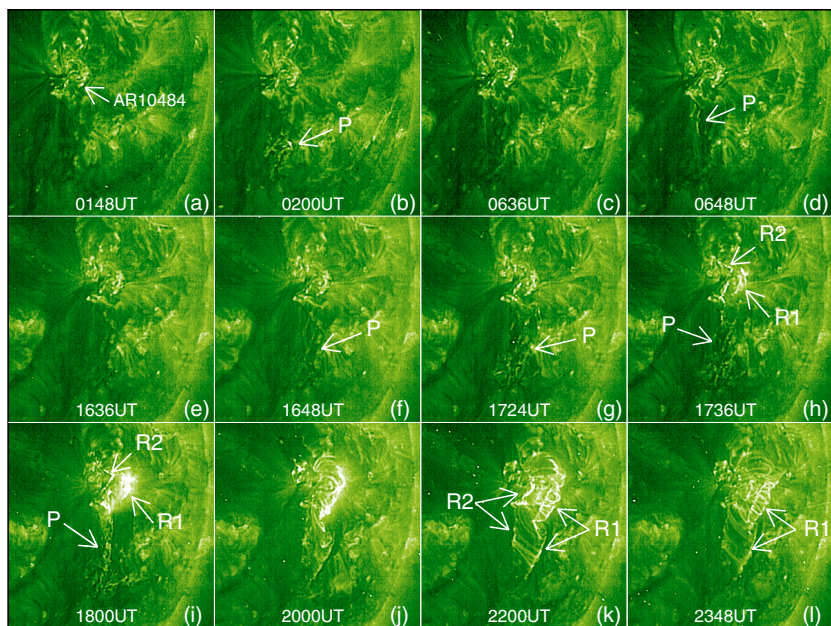


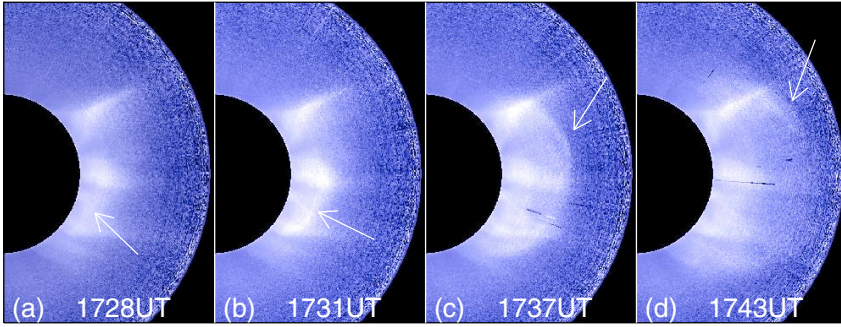
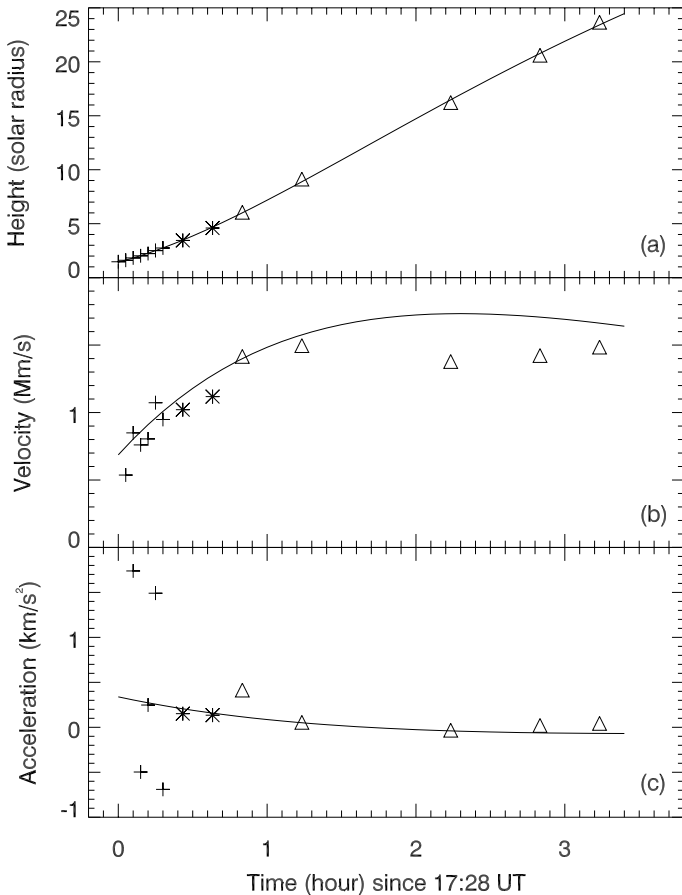
**Fig. 9.** Time sequence of the X1.2 X-ray flare on AR 10484 as recorded in EIT 195 Å. The images have been contrast-enhanced with the WICE technique. a)–d) The sudden brightenings (arrow P) indicate small scale activity during more than ten hours prior to the X1.2 flare. e)–f) The small scale eruption-like activity appeared about half hour before the X1.2 flare occurred. g)–l) The evolution of flare ribbons (indicated by arrow R1 and R2) after the X-ray flare.

on-disk activity. In the present work, the enhanced EIT 195 Å images show some typical morphological features of the two-ribbon flare scenario when F1 and F2 erupted (later CME1 and CME2). This suggests that improvements in detecting techniques may help build up CME-on-disk-activity correlations more easily. The signatures observed in EIT images for these two events are similar to those of the X1.2 X-ray flare associated with CME4 (compare e.g. Figs. 3c through 3j and Figs. 5e through 5j with Figs. 9h through 9l). The similarity of the

signatures observed indicates that the three events underwent a similar physical process somehow associated with magnetic reconnection (flare ribbons and loop systems represent one of the best evidences of magnetic reconnection in the solar atmosphere; see e.g. Forbes & Acton 1996; Forbes 2000; Priest & Forbes 2002; Lin et al. 2003). Of course, the flare ribbons and post-flare loops observed during events 1 and 2 looked much weaker than those of the X1.2 X-ray flare in the EIT 195 Å images. This may be due to the fact that F1 and F2 were located in a quiet sun

**Table 2.** Main characteristics of the four events.

CMEs	Speed at $\sim 2 R_{\odot}$ ( $\text{km s}^{-1}$ )	Final speed ( $\text{km s}^{-1}$ )	Acceleration range ( $R_{\odot}$ )	Flare strength	On-disk activity
CME1	318	390	2.0	C 3.8	filament eruption and flare
CME2	567	724	8.0	C 2.2	filament eruption and flare
CME3	43	400	30.0	–	none
CME4	668	1827	5.0	X 1.2	flare

**Fig. 10.** Time sequence of the CME (CME4) associated with the X1.2 flare as recorded by the MK4 coronagraph. The white arrows indicate the leading edge of CME4. **a)** The leading edge started to form at 17:28 UT. **b)** The leading edge of CME4 clearly formed at 17:31 UT. **c)** The angular span of CME4 increased significantly within 6 min. **d)** The angular span of CME4 reached about  $117^{\circ}$ .**Fig. 11.** Time-profiles of the altitude **a)**, velocity **b)** and acceleration **c)** of the CME4 leading edge appearing in FOV of MK4 (+), C2 (\*) and C3 ( $\Delta$ ), respectively. The solid curves indicate the fitting result to the data according to Eq. (1).

region (spotless) where the available free energy to drive the eruption was limited (Vršnak et al. 2005).

The curves that describe the kinematical behavior of CME1, CME2 and CME4 display common features. Though its

final speed is less than  $200 \text{ km s}^{-1}$ , the CME event associated to F1 experienced a rapid increase in speed with an acceleration of up to  $50 \text{ m s}^{-2}$  for about two hours before appearing in the C2 FOV (Fig. 4c). Afterward, the acceleration vanished. The event associated to F2 underwent an apparent acceleration of  $\sim 35.2 \text{ m s}^{-2}$  in the early stage of its development ( $1-5 R_{\odot}$ ). After appearing in the C2 FOV ( $>4 R_{\odot}$ ), the associated CME exhibited a smaller acceleration ( $\sim 15.4 \text{ m s}^{-2}$ ). The propagation of CME4 presented more impulsive characteristics: its average acceleration reached up to  $330 \text{ m s}^{-2}$  in the first 30 min, decreasing to less than  $70 \text{ m s}^{-2}$  after appearing in the C2 FOV. In spite of their different final speeds, these three events all experienced an apparent acceleration of impulsive fashion during the early stage. On the other hand, the motion of CME3 manifested a relatively smooth acceleration of about  $5.6 \text{ m s}^{-2}$  during the whole process.

Therefore, CME3 was an exception and the kinematic characteristics of the other three events are not very consistent with the concept of only two distinct classes of CMEs, where fast CMEs tend to decelerate while slow CMEs tend to accelerate. Recent statistical studies also show that there are some exceptions to the two-classes of CMEs scenario (Vršnak et al. 2005). Moon et al. (2004) studied a fast CME that developed from a helmet streamer and exhibited apparent acceleration in the altitude range from 2 to  $11 R_{\odot}$ . They speculated that the eruption is related to the destabilization of the helmet streamer. Generally, the two types of CMEs could be regarded as a statistical concept or two types of tendencies. Actually, the speed and acceleration of CMEs may depend on several physical characteristics such as flare strength, magnetic free energy, magnetic field configuration (open or partially open), projection effects, etc. Our results suggest that both slow and fast CMEs could experience apparent acceleration in the lower corona followed by a significant acceleration decrease in the higher corona. In particular, the motion of CME1 displayed acceleration at the beginning followed by a deceleration later on. Instead, the others remained accelerated.

Thus, the above results suggest that our current understanding of the CME-flare correlation needs to be modified and improved. Generally, it is still true that fast CMEs, such as CME4, are usually associated with major flares, while slow CMEs,

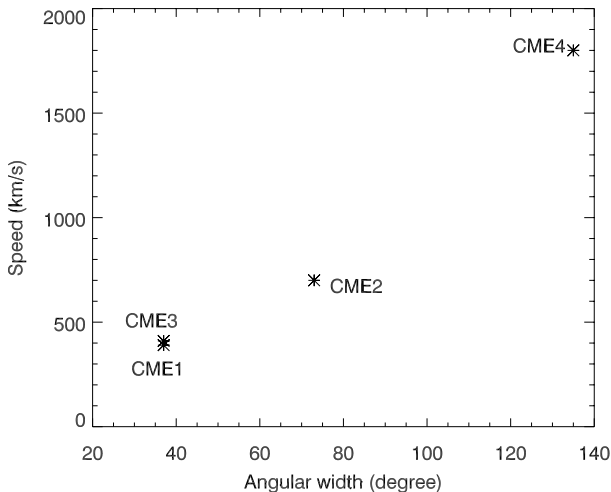


**Fig. 12.** Plot of CME speeds versus their angular widths.

such CME1 and CME2, are closely related to eruptive filaments (Sheeley et al. 1999). In the present study, as was the case for CME1, CME2 is associated with the eruption of a filament (short instead of long). However, its speed resulted larger than  $700 \text{ km s}^{-1}$ . Although CME3 is slightly faster than CME1, the EUV images show clear on-disk activities associated with CME1, while CME3 slowly developed from the disruption of a pre-existing helmet streamer without any apparent signature on the solar disk. All these facts reveal that the CME speed and acceleration may be related not only to the flare class, but to other parameters as well.

When analyzing the size of each CME, we noticed that the speeds of the four CMEs manifested correlation to their angular widths. The angular width of the slowest CME, i.e. CME1, is only  $37^\circ$ , the angular width of CME2 was about  $73^\circ$ , and that of CME4 was more than  $135^\circ$ . Though the angular width of the disrupting magnetic arcade associated with CME3 is larger than  $110^\circ$ , it is not the expansion of CME3's lateral edge. Instead, the angular width of CME3's trumpet-shape structure in LASCO C3 image is only  $37^\circ$  (compare the angular scales of the two features shown in Fig. 71). Figure 12 plots the CME speed against the CME angular width for the four events investigated in the present work. It displays an apparent linear relation of the CME speed to the angular width. Recent statistical studies by Yashiro et al. (2004) of CMEs observed by LASCO from 1996 to 2002 also indicated that there is a weak correlation between CME speed and angular width.

We must point out that although both CME1 and CME3 were slow CMEs, their morphological features and kinematic characteristics are quite different: CME1 developed from an eruptive prominence and was associated with a two-ribbon flare observed in EIT 195 Å, and CME3 sprouted from a helmet streamer and was quite similar to the so-called “streamer blowout” events. Unlike CME1 (event that exhibited a clear three-component structure), CME3 had no clear trailing edge or dark cavity. This type of event were called “curved front” CMEs by Howard et al. (1985). CME3 had a constant acceleration of about  $5.6 \text{ m s}^{-2}$  all along its development. After CME2 deflected the streamer, it swayed laterally at first, then bulged, and finally ejected the material in the streamer. This event was not correlated with any on-disk activity. We have examined the EIT 195 Å images both in the solar disk and out of the limb, and failed to identify any signature associated with CME3. So, the possibility of eruptive activities on the back-side of the Sun is slim. Unlike the other

three CMEs, this CME did not show either increase or decrease in acceleration during the whole process. It behaved as a real gradual event. This CME took off at a higher altitude ( $>2 R_\odot$ ), where the gas pressure in the solar wind dominates that of the magnetic field. Therefore, it is quite possible that its initiation might result from the destruction of the relevant magnetic structure by the solar wind.

On the other hand, CME1 was associated with a two-ribbon flare of typical morphological features. However, CME1 itself was slow and the flare small. So, the relevant eruption was very likely to be triggered by the loss of equilibrium in the magnetic structure. Only because the free energy (the difference between the total energy in the disrupting magnetic field and that in the corresponding potential field) in the configuration prior to the eruption was low, did the eruption develop a slow CME and a small two-ribbon flare (e.g., see discussions Lin 2004b). Although F2 is shorter than F1, the speed of CME2 was higher, and the flare ribbons after the F2 eruption appeared brighter and more compact than those of F1. This suggests that the free energy driving the F2 eruption is more than that driving F1. Since the CME2 ejected immediately after the eruption of CME1, the relative high speed of CME2 may also be due to the removal of the two inward forces acting on F2, which are caused by the overlying magnetic field and the dragging material, respectively.

Finally, three decades of observations have shown that CMEs exhibit much more complex features than expected. Obviously, the study of the four CMEs in this work is far from enough to cover all characteristics of CMEs. To draw a more definite conclusion of CMEs, the following studies may be suggested. First, the statistical study of the kinematic characteristics of CMEs, especially in the range of the low corona (e.g.  $0-5 R_\odot$  above solar surface), where most CMEs seem to accelerate. Second, and in order to improve our knowledge of how CMEs interact with helmet streamers, more examples of “streamer blowout” events need to be examined jointly with the corresponding, if any, on-disk activities, such as the recent study of Gibson et al. (2006). In addition, individual case studies, such as X-class flares without CMEs, CMEs without on-disk signatures, and events with various well observed features (e.g. Bao et al. 2006), are key to look into the CMEs as a whole physical process comprehensively.

*Acknowledgements.* We thank M. Zhang for providing the MLSO MK4 images. This work was supported by the National Natural Science Foundation of China under grants 10233050, 10373016 and 10473016, the Ministry of Science and Technology of China under the 973 Program grant 2006CB806300, and the National Basic Research Program of China under grants TG 2000078400 and TG 2000078401 to the National Astronomical Observatories of China. J.L.'s work at CfA was supported by NASA under grants NNG06GI88G to the Smithsonian Astrophysical Observatory. *SOHO* is a joint mission of the European Space Agency and the US National Aeronautics and Space Administration.

## References

- Andrews, M. D., & Howard, R. A. 2001, *SSRv*, 95, 147
- Bao, X., Zhang, H., & Lin, J. 2006, *Chinese J. Astron. Astrophys.*, 6, 741
- Dere, K. P., Brueckner, G. E., Howard, R. A., Michels, D. J., & Delaboudiniere, J. P. 1999, *ApJ*, 516, 465
- Forbes, T. G. 2000, *J. Geophys. Res.*, 105, 23153
- Forbes, T. G., & Acton, L. W. 1996, *ApJ*, 450, 330
- Gibson, S. E., Foster, D., Burckpile, J., de Toma, G., & Stanger, A. 2006, *ApJ*, 641, 590
- Gilbert, H. R., Holzer, T. E., Burckpile, J. T., & Hundhausen, A. J. 2000, *ApJ*, 537, 503
- Gopalswamy, N., Shimojo, M., Lu, W., et al. 2004, *Adv. Space Res.*, 33, 676

- Gosling, J. T., Hildner, E., MacQueen, R. M., et al. 1974, *J. Geophys. Res.*, 79, 4581
- Gosling, J. T., Hildner, E., MacQueen, R. M., et al. 1976, *Sol. Phys.*, 48, 389
- Harrison, R. A. 1991, *Adv. Space Rev.*, 11, 25
- Harrison, R. A. 1995, *A&A*, 304, 585
- Howard, R. A., Sheeley Jr., N. R., Michels, D. J., & Koomen, M. J. 1985, *J. Geophys. Res.*, 90, 8173
- Hundhausen, A. J. 1988, In Pizzo, V., et al. ed. *Proc. Sixth International Solar Wind Conf. NCAR TN-306*, 1, 181
- Hundhausen, A. J. 1993, *J. Geophys. Res.*, 98(A8), 13177
- Klimchuk, J. A. 2001, in *Space Weather*, AGU Monograph, ed. P. Song, G. Siscoe, & H. Singer, 125, PP. 143-157
- Lin, J., Soon, W., & Baliunas, S. L. 2003, *New A Rev.*, 47, 53
- Lin, J. 2004, *Sol. Phys.*, 222, 115
- Lin, J., Raymond, J. C., & van Ballegoijen, A. A. 2004, *ApJ*, 602, 422
- MacQueen, R. M., & Fisher, R. R. 1983, *Sol. Phys.*, 89, 89
- Moon, Y.-J., Choe, G. S., Wang, H., et al. 2002, *ApJ*, 581, 694
- Moon, Y.-J., Cho, K. S., Smith, Z., et al. 2004, *ApJ*, 615, 1011
- Munro, R. H., Gosling, J. T., Hildner, E., et al. 1979, *Sol. Phys.*, 61, 201
- Plunkett, S. P., Michels, D. J., Howard, R. A., et al. 2002, *Adv. Space Rev.*, 29, 1473
- Priest, E. R., & Forbes, T. G. 2002, *A&A Rev.*, 10, 313
- Raymond, J. C., Ciaravella, A., Dobrzycka, D., et al. 2003, *ApJ*, 597, 1106
- Sheeley Jr., N. R., Howard, R. A., Koomen, M. J., et al. 1982, *Space Sci. Rev.*, 33, 219
- Sheeley Jr., N. R., Walters, J. H., Wang, Y.-M., & Howard, R. A. 1999, *J. Geophys. Res.*, 104(A11), 24739
- Starck, J.-L., Siebenmorgen, R., & Gredel, R. 1997, *A&A*, 482, 1011
- St. Cyr, O. C., & Web, D. F. 1991, *Sol. Phys.*, 136, 379
- St. Cyr, O. C., Howard, R. A., Simnett, G. M., et al. 1997, *Proc. 31st ESLAB Symp., Correlated Phenomena at the Sun, in the heliosphere and in Geospace*
- Stenborg, G. A., & Cobelli, P. 2003, *ApJ*, 398, 1185
- Subramanian, P., Dere, K. P., Rich, N. B., & Howard, R. A. 1999, *J. Geophys. Res.*, 104(A10), 22321
- Tousey, R. 1973, In *Space Research XIII*, ed. M. J. Rycroft, & S. K. Runcorn (Berlin: Akademie-Verlag), 173
- Vršnak, B., Sudar, D., & Ruždjak, D. 2005, *A&A*, 435, 1149
- Yashiro, S., Gopalswamy, N., Michalek, G., et al. 2004, *J. Geophys. Res.*, 109(A7), 7105
- Zhang, J., Dere, K. P., Howard, R. A., Kundu, M. R., & White, S. M. 2001, *ApJ*, 559, 452
- Zhang, J., Dere, K. P., Howard, R. A., & Vourlidas, A. 2004, *ApJ*, 604, 420
- Zhang, M., Golub, L., DeLuca, E., & Burkepile, J. 2002, *ApJ*, 574, L97